Journal of Applied Electrochemistry (2005) 35:589–598
DOI 10.1007/s10800-005-2321-4
© Springer 2005

Simulation and experimental determination of the macro-scale layer thickness distribution of electrodeposited Cu-line patterns on a wafer substrate

KAREN PANTLEON[1], BART VAN DEN BOSSCHE[2,*], MARIUS PURCAR[2], PAOLO BARIANI[1] and GERT FLORIDOR[2]
[1]*Department of Manufacturing Engineering and Management, Technical University of Denmark, Building 204, Lyngby 2800, Denmark*
[2]*Department of Electrical Engineering, Vrije Universiteit Brussel, Pleinlaan 2, Brussels 1050, Belgium*
*(*author for correspondence, tel.: +32-2-6293466; fax: +32-2-6293620; e-mail: bvdbos@vub.ac.be)*

Received 9 September 2004; accepted in revised form 31 January 2005

Key words: atomic force microscopy, copper plating, current density distribution, numerical simulation, patterned wafer, X-ray fluorescence microscopy

Abstract

The impact of adjacent patterned zones with different active area densities on the current density and electrodeposited layer thickness distribution over a wafer substrate is examined, both by experiment and numerical simulation. The experiments consist in running an acid copper plating process on the patterned wafer, and layer thickness measurements by means of X-ray fluorescence (XRF) and atomic force microscopy (AFM). The simulations are based on a potential model approach taking into account electrolyte ohmic drop and electrode polarization effects, combined to a boundary element method (BEM) approach to compute the current density distribution over the electrodes. Experimental and computed layer thickness distributions are in very good agreement.

List of Symbols

$\bar{l}_n$	inward unity vector normal to the electrode surface
A	polarization conductance (300 Ω^{-1} m^{-2})
B	polarization current density offset (0.0 A m^{-2})
d	thickness of the metallic electrode layer (m)
E_{01}	equilibrium potential for the deposition reaction $Me^{z+} + ze^- \rightarrow$ Me (0.2 V vs. NHE)
E_{02}	equilibrium potential for the anodic oxygen evolution reaction (1.5 V vs. NHE)
F	Faraday constant (96 500 C mol^{-1})
j	amplitude of current density in the electrolyte (A m^{-2})
j_n	amplitude of current density normal to the electrode surface (A m^{-2})
M	atomic metal weight (65 g mol^{-1})
Q	inward flux normal to the boundary Γ(V m^{-1})
U	electrolyte potential (V)
V	electrode potential (V)
z	number of electrons exchanged in the metal deposition reaction (2)
σ	specific conductivity of the electrolyte (20 Ω^{-1} m^{-1})
ρ	metal deposit density ($8.0E+6$ g m^{-3})
Γ	bounding surface enclosing the electrolyte domain
Γ_j	surface of a triangular element
Δt	plating time (s)
$[H]$	BEM potential matrix
$[G]$	BEM flux matrix
$[I]$	diagonal unity matrix
AX	axisymmetrical
2D	two dimensional
3D	three dimensional
RDE	rotating disc electrode
CPU	central processor unit
BEM	boundary element method
FEM	finite element method
PC	personal computer

1. Introduction

The implementation of electrochemical deposition in various microfabrication technologies and the proceeding miniaturization of feature sizes in microelectronics, sensor and actuator technology require improved thickness uniformity of electrodeposits. The ability to control the macro-scale uniformity of electrodeposition on a

carrier (e.g. a wafer) is the key to successful application of electrodeposition technologies, because uniformity is essential to meet functional and dimension requirements on the features.

Of special importance during electrodeposition is the local current density at the cathode and its distribution, because this directly affects the thickness uniformity of the electrodeposit. On the basis of long ranging experiences of electrodeposition onto plain, i.e. non-patterned, substrates the distribution of the current density over the sample surface can be well-controlled and for such electrodeposits acceptable thickness uniformity is usually obtained. Well-known edge effects, i.e. largest thickness close to edges and corners, can be minimized by means of auxiliary cathodes (current thieves) [1].

For electrodeposition onto patterned substrates, controlling the thickness uniformity becomes complicated since it is influenced by various effects. The ability of gap-filling, which is required from the electrolyte in the case of patterned substrates, is attributed to the presence of various additives and their competitive interaction. Of particular interest and industrial relevance is a combination of three organic additives – chloride, polyethylene glycol (PEG) and 3-mercapto-l-propanesulfonate (MPSA) – in an acidic Cu-electrolyte. Strong synergetic effects between these additives (Cl^- + PEG inhibit, while MPSA accelerates the deposition process) are reported [2–6]. Not only the interplay between electrolyte composition and pattern geometry determines the filling degree of individual gaps, rather the pattern itself can affect the growth characteristics. For example, the particular distribution of the resist material in through-mask-plating may exert an influence on the current density distribution and, hence, the thickness of the deposits [7–9].

Tailored growth of patterned electrodeposits is still a challenge, because of the specific interaction between various parameters, among them the pattern geometry, current thief, distance between anode and cathode, electrolyte composition, agitation and temperature, applied current density and the substrate (seed) material. Experimental studies [10] indicate that deposition parameters that had contributed positively to current density uniformity when assessed individually did not produce the expected synergetic effect with respect to uniformity improvement. Hence, theoretical modeling has become increasingly important for simulating the current density and deposit thickness distribution on patterned surfaces.

For plating applications involving only plain electrodes, current density distributions can often be simulated over a two dimensional (2D) or axisymmetrical (AX) symmetry plane of the plating tank configuration. With patterned electrodes, however, a full three dimensional (3D) approach is almost always required. Only a limited number of publications deal with 3D current density distribution simulations in electrochemical plating reactors [11–15]. Most simulations presented in the literature are based on a boundary element method (BEM) approach and/or finite element modeling (FEM) to compute the current density distributions both on patterned and non-patterned surfaces. Recently, some of the present authors applied a combined BEM–FEM numerical approach for the 3D-simulation of the current density distribution for a patterned wafer [16]. The pattern on the wafer was approximated by an outer zone covered with a photoresist, and an inner zone that was assumed to be a plain electrode.

The present paper reports on the thickness uniformity of free-standing Cu-line patterns with various geometries, as manufactured on a wafer applying photo-lithography and subsequent electrochemical deposition. Numerical simulation of the current density distribution was carried out for different line patterns applying a 3D potential model combined to a BEM solution technique. The thickness distribution was calculated from the simulated current density distribution and compared with the experimentally determined thickness distribution as obtained from X-ray fluorescence analysis and atomic force microscopy.

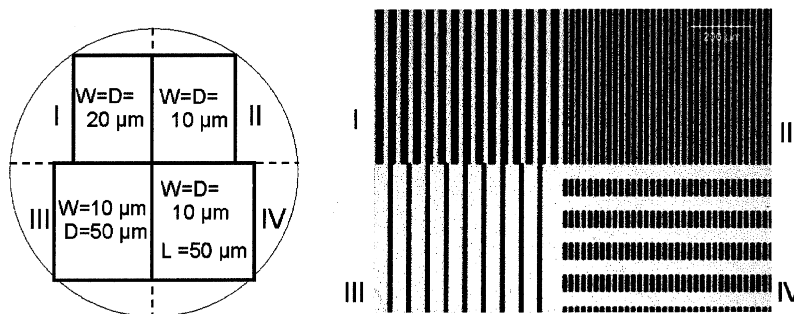

Fig. 1. Geometry of different line patterns arranged on a wafer surface. Scheme showing the arrangement of the various patterns (I–IV) on the wafer and the corresponding geometries: Line width *W*, separation *D* between neighboring lines, line length *L* (left). Optical microscopy image from the center of the wafer (right).

2. Experiments

2.1. *Manufacturing of free-standing line patterns*

As plating base, a 100 nm thick Au-layer was deposited by means of physical vapor deposition on a glass wafer (diameter 100 mm). In a clean room atmosphere, a suitable photoresist (positive resist, type AZ 4562/Höchst) was spun on the surface to a thickness of 6.5 μm. Applying UV-photo-lithography (i.e. illuminating the resist with UV-light through a patterned mask projected on the surface and developing the exposed resist) a 3D resist pattern was obtained on the wafer (cf. [17]).

Several line patterns with varying line widths and interline distances were arranged in four different zones (I, II, III, IV) on the wafer, as shown in Figure 1. Line widths of 10 and 20 μm, respectively, were applied and interline distances varied between 10, 20 and 50 μm. Consequently, the four different zones on the wafer contained several hundreds of parallel lines (I: 675 lines, II: 1350 lines, III: 580 lines, IV: 1750 lines), While lines in the zones I, II and III can be considered as infinitely long, lines in zone IV were limited in length to 50 μm.

Electrochemical deposition was carried out from a Cu-electrolyte containing 0.56 mol l^{-1} $CuSO_4 \cdot 5H_2O$, 1.4 mol l^{-1} H_2SO_4, 1.1 $\times$ 10^{-3} mol l^{-1} Cl^-, 8.8 $\times$ 10^{-5} mol l^{-1} polyethylene glycol (PEG, average molar mass of 3400 g/mol) and 1.5 $\times$ 10^{-3} mol l^{-1} 3-mercapto-1-propanesulfonate (MPSA). During electrodeposition, the wafer was placed in a wafer holder and positioned vertically in a rectangular reactor with the anode at the opposite side of the wafer (Figure 2). A ring shaped current thief was placed around the wafer during deposition. Three electrical contact clips were mounted on the holder, ensuring connection of the wafer with the current source, and, at the same time, contacting the wafer with the current thief. A mean current density of 200 A m^{-2} was applied at the cathode (patterns and contacts on the wafer). This corresponds to a current of 0.49 A. The total current through the anode (1.04 A) was adjusted in order to achieve this current value on the cathode. Electrodeposition was carried out for a period of 5.5 min at room temperature, while establishing vigorous air agitation of the electrolyte.

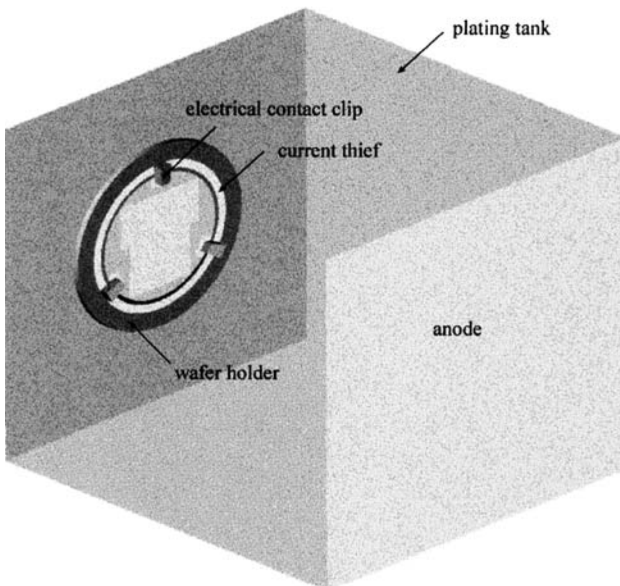

Fig. 2. Plating tank configuration.

2.2. *Experimental thickness determination*

The uniformity of the film thickness over the wafer was investigated applying X-ray fluorescence (XRF) measurements by means of a Fischerscope X-Ray System XDVM-W with WinFTM software based on the fundamental parameter method allowing for standard-free measurements. For X-ray fluorescence analysis the samples were defined as film–substrate systems with a double layer of Au and Cu on a glass substrate. The primary radiation, as emitted from a micro-focal tungsten X-ray tube, excited both layers (Cu and Au) to emit their characteristic X-ray fluorescence radiation, which was detected by a Xenon gas filled proportional counter. XRF-analysis was performed at distinct positions on the wafer (mapping with steps sizes of 4 mm in x- and y-direction, respectively). A measurement time of 20 s per point was used. Applying a suitable collimator, the X-ray fluorescence spectrum was obtained from a spot size with diameter of about 0.2 mm, i.e. the measurement averages over several lines. For the various patterns, the relative contribution of the Au-layer to the measured fluorescence spectrum depends on the respective pattern geometry (line-widths, -lengths and inter-line distances). Therefore, a correction was applied to the apparent thickness of the Cu-lines taking into account the actual area fraction of Cu-lines in the different zones and the pattern dependent absorption of X-rays.

Additionally, atomic force microscopy (AFM, Danish Micro Engineering DS 95-200) was used for thickness determination on 42 selected positions within the line patterns on the wafer. The AFM was operated in the non-contact mode (AC) with a tip vibration at a frequency of about 300 kHz close to the surface and a probing force of 0.1 nN. The total scan area at the individual measurement positions (dimension: horizontally $\times$ vertically) was either 22×10 μm^2 (zone I) or 12×10 μm^2 (zones II, III, IV). The deposit thickness was determined as described below. AFM images were calibrated to achieve the best possible measurement accuracy. In particular the determination of the appropriate vertical scaling factor had been previously obtained by the use of transfer standards featuring step heights. Compensation of any slight installation slope and thermal drift along the slow scanning direction was performed by off-line image processing techniques. The deposition depth was then measured on the profile resulting from averaging over the 64 single scan lines within each of the AFM images.

Table 1. Active-area-fraction for patterned zones and contacts

Zone	Zone dimension length × width/m × m	Zone area/m^2	Active-area-fraction θ
I	0.027 × 0.042	1.107×10^{-3}	0.500
II	0.027 × 0.042	1.107×10^{-3}	0.500
III	0.035 × 0.035	1.225×10^{-3}	0.167
IV	0.035 × 0.035	1.225×10^{-3}	0.250
Contacts	0.010 × 0.010	1.000×10^{-3}	1.000

3. Simulation

Simulations were performed with the software tool presented in [16]. The model accounted for ohmic drop effects in the electrolyte solution and the electrode polarization including the active area density of the different patterns. The simulations did not take into account the internal resistivity of the wafer and the type of substrate material. Furthermore, attributes specific to the individual lines that constitute the patterns were disregarded. The validity of the later assumption was proven in an additional simulation on a micro-scale for the effect of an individual line (cf. Section 4.1).

3.1. *Mathematical model*

The patterned wafer was described in terms of the active-area-fraction not covered with photoresist. Table 1 summarizes the active-area-fraction θ for the different zones containing various line patterns (cf. Figure 1) and for the electrical contacts.

3.1.1. *Cathodic reaction*

The polarization behavior for single metal deposition processes $Me^{z+} + ze^- \rightarrow Me$ is often quite accurately described by a Butler–Volmer type relation [18], but for the simulations in this paper, a more straightforward approach is used. The measured cathodic polarization data (cf. Section 3.3) are transformed into a continuous spline curve, which is directly used as a boundary condition for the simulations:

$$j_n = \theta f(V - U - E_{01}), \qquad (1)$$

where j_n is the amplitude of current density normal to the electrode surface, V the electrode potential, U the electrolyte potential, and E_{01} the equilibrium potential for the deposition reaction. For an electrode surface covered with very small features (micro-size range), the remaining parts insulating (photoresist) the effect of a surface active fraction θ being <1, can simply be encompassed in expression (1), since the current density distribution on the micro-scale features is uniform (as shown in Section 4.1). This approach was also followed by Mehdizadeh et al. [7].

3.1.2. *Anodic reaction*

The main reaction that occurs at inert impressed current anodes is oxygen evolution. Due to the thin passivation layer that is often present on the surface of this type of electrodes, the polarization behavior is approached by a linear relation:

$$j_n = A(V - U - E_{02}) + B, \qquad (2)$$

with A, B polarization constants and E_{02} the equilibrium potential for the oxygen evolution reaction. Anode polarization effects are of minor importance – at least from a modeling point of view – if the anodes are at respectable distance from the cathode surface, which was the case here.

3.1.3. *Electrolyte*

It was assumed that the electrolyte was well stirred or refreshed, hence did not suffer from any mass transport problems, and only charge transport with normal ohmic resistivity effects is to be considered. Hence the potential model holds, being described by the Laplace equation for the electrolyte potential U:

$$\overline{\nabla}(\bar{j}) = 0 \quad \bar{j} = -\sigma\overline{\nabla}U. \qquad (3)$$

At insulating boundaries, the current density perpendicular to the surface should be zero, which results in the following boundary condition:

$$\overline{j \cdot 1_n} = j_n = -\sigma\overline{\nabla}U \cdot \bar{1}_n = \sigma Q = 0. \qquad (4)$$

At electrodes, j_n is given by equations of type (1) or (2).

3.2. *Numerical solution method*

3.2.1. *BEM approach for electrolyte and electrode reactions*

As the conductivity of the electrolyte was constant, the BEM is to be preferred over other (volume) discretization methods as for example FEM or the finite difference method (FDM), to solve the simplified charge conservation equation (3). When the BEM is applied, only the boundaries of the domain must be discretized. Another advantage, in particular for electrochemical systems, is that the current density distribution along the electrodes is a direct unknown to the problem, rather than a variable that has to be computed afterwards from the derivative of the potential field perpendicularly to the electrodes. This implicates that BEM is the more accurate method for the present problem, compared to FEM or FDM.

The typical BEM equation for the contribution at a point i is [19, 20]:

$$c^i U^i + \int_\Gamma U \frac{\partial w^*}{\partial x} d\Gamma = \int_\Gamma w^* Q d\Gamma, \qquad (5)$$

with $w^* = 1/4\pi r$ the 3D Green function (r being the position relative to point i) and the inward flux $Q = \partial U/\partial n$ on the boundary nodes. c^i is an integration constant for point i. Γ is the 2D surface that encloses the 3D computational domain. In order to apply BEM, the boundary Γ is to be discretized into a series of N non-overlapping elements, transforming Equation 5 into:

$$c^i U^i + \sum_{k=1}^{N} \int_{\Gamma_k} U \frac{\partial w^*}{\partial x} d\Gamma = \sum_{k=1}^{N} \int_{\Gamma_k} w^* Q d\Gamma. \quad (6)$$

The index k ranges over all elements of the domain and integration was performed over the surface Γ_k of each element, For the 3D BEM computations in this paper, triangular elements with linear shape functions for the unknown potential U and flux field it Q were used, restricting the unknowns to the nodal values.

Taking into account Equation 6, the BEM equations are expressed in matrix form:

$$[H] \cdot \{U\} = [G] \cdot \{Q\} \quad (7)$$

with $\{U\}$ and $\{Q\}$ unknown vectors of size N. The matrices H and G in Equation 7 are fully populated and depend only on the geometry of the domain. The system equation matrixs

$$\begin{bmatrix} [H] & 1/\sigma[-G] \\ [0] & [I] \end{bmatrix} \begin{Bmatrix} \{U\} \\ \{j_n\} \end{Bmatrix} + \begin{Bmatrix} \{0\} \\ \{f(V-U)\} \text{ or } \{0\} \end{Bmatrix} = 0 \quad (8)$$

is non-linear due to the presence of non-linear polarization relations $f(V-U)$ of type (1). It was solved using a Newton–Raphson iterative method, combined with a band Gauss algorithm [21] to solve the linear system of equations that appears after each iteration of the Newton–Raphson procedure.

3.2.2. *Triangular surface mesh generation*
The grid quality is of utmost importance for the accuracy of the results. A hybrid grid generator was used to produce the surface mesh required for the BEM computations [22].

3.3. *Physico-chemical input parameters*

In order to produce reliable simulation results, the physico-chemical input parameters need to be defined carefully. The necessary data were experimentally determined for the applied electrolyte. The electrical conductivity σ was measured with a high frequency (0.1 MHz) impedance measurement at a rotating disc electrode (RDE) and amounted to 43.1 S/m at 27 °C. Polarization investigations at this temperature were performed at a an RDE at 4000 rpm for a bath that was saturated with nitrogen gas. A Pt mesh electrode was used as counter electrode and the applied potential was referenced vs. an Ag/AgCl electrode containing a saturated KCl solution. Point by point polarization measurements were obtained by imposing a series of electrode potentials on a Pt RDE, and recording the current response for a certain time until the steady-state current was reached. The applied potentials were corrected for the ohmic resistance of the electrolyte around the RDE. Values as plotted in Figure 3 were used for the current density distributions as simulated in this paper.

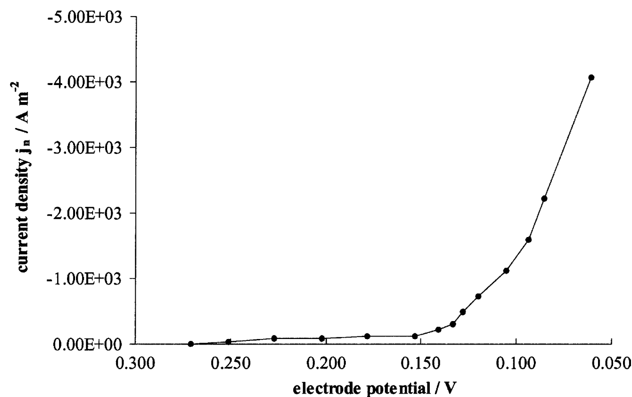

Fig. 3. Point-by-point measured cathodic copper deposition polarization curve at 4000 rpm, after correction for ohmic drop around the RDE.

4. Simulated current density distributions

4.1. *Micro-scale simulation*

First, it was examined whether the current density distribution on a single micro-scale feature is uniform. This is a crucial assumption for the translation of the local pattern geometry into a simple active surface fraction factor θ that can be incorporated in Equation 1. The current density distribution over one single feature of pattern IV was simulated for different mean current densities. Due to the micro-scale symmetry, only one quarter of the feature and surrounding photoresist was

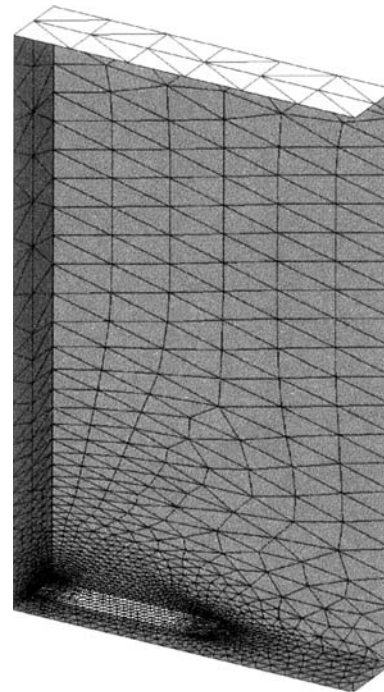

Fig. 4. Configuration and boundary mesh for the micro-scale simulations, white bottom rectangle represents 1/4 of a pattern (zone IV); vertical boundaries (only 2 out of 4 are shown) are symmetry planes. Top plane represents a virtual counter electrode.

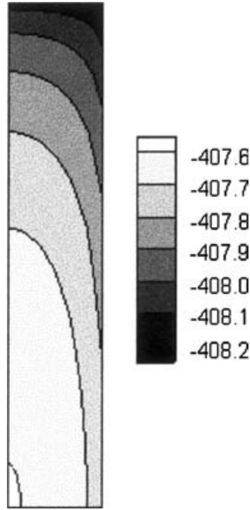

Fig. 5. Micro-scale current density distribution for pattern IV (quarter part, bottom left corresponds to center of the pattern) for an average current density of -407.8 A m^{-2}.

considered (Figure 4). The computed results are presented in Figure 5, indicating a uniform current density distribution down to a variation of 0.1%. This conclusion can easily be transferred to the patterned zones I, II and III.

4.2. *Macro-scale simulation*

Macro-scale computations were performed for the entire reactor configuration. The surface mesh used for the BEM computations is visualized in Figure 6. Geometrical simplifications (e.g. the wafer holder attachment arm is not considered) significantly reduce the number of elements and nodes of the triangular mesh. The number of elements was further restricted by use of a coarse structured (e.g. the wafer holder) or unstructured (e.g. the vertical side walls) mesh for the reactor surfaces that do not belong to the wafer, finally facilitating calculations on a normal PC within acceptable CPU times (about 40 min on a 2.5 GHz, 1.5 GB RAM PC). The mesh consisted of 33 014 elements and 18 786 nodes.

Table 2 contains an overview of the current received by each patterned zone, the contact zones and the current thief. Figure 7 shows the simulated current density distribution over the patterned zones.

5. Thickness distribution

5.1. *Determination of the thickness distribution from the simulation*

The local pattern deposit thickness d after a certain process time Δt was calculated from the simulated current density j_n from Faraday's law:

$$\Delta d = \frac{M \Delta t j_n}{\theta \rho z F}, \tag{9}$$

assuming a 100% efficiency for the copper deposition process, with the atomic weight of the metal $M = 65$ g mol^{-1}, the deposit density $\rho = 8.0\times 10^6$ g m^{-3} the number of electrons exchanged in the metal deposition reaction $z = 2$, Faraday's constant $F = 96\,500$ C mol^{-1}. The active area density θ is taken from Table 1 and j_n, represents the local computed current density on the cathode surface (cf. Figure 7). The obtained layer thickness distribution for a plating time $\Delta t = 5.5$ min is plotted in Figure 8.

5.2. *Experimentally determined thickness distribution*

Figure 9 shows the distribution of the deposit thickness as experimentally determined by XRF analysis for Cu-line patterns in the four different zones on the wafer. Results of local thickness measurements carried out with the AFM on selected positions on the wafer are shown in Figure 10. A comparison between AFM- and XRF-results reveals that AFM-measurements generally resulted in slightly higher thickness values, but for both techniques the same thickness ratios between the different patterns were obtained. Differences between the individual thickness values determined with AFM and XRF are related to the different information content of both techniques; XRF provides average values over several lines and data have been absorption corrected, while AFM yields local direct measurements with fewer statistics.

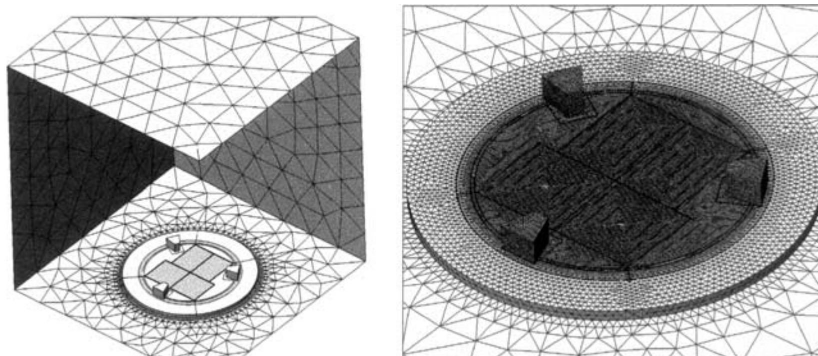

Fig. 6. Triangular surface mesh of the entire reactor configuation (left) and (b) a detailed view of the wafer (right).

Table 2. Current received by the distinct electro-active surfaces

	Current/A
Zone I	−0.119
Zone II	−0.120
Zone III	−0.083
Zone IV	−0.100
Contact zones	−0.066
Current thief	−0.55

5.3. *Comparison between simulation and experiment*

Comparison between the simulated thickness distribution (Figure 8) and the experimentally determined distribution of the deposit thickness over the wafer (Figures 9 and 10) reveals a very good agreement (above 90% accuracy) between 3D-simulations and experiments. Both the thickness distribution within individual patterned zones and in the center of the wafer, where the four zones meet, is well-predicted by the simulation results.

However, some discrepancies larger than 10% exist in terms of the absolute thickness values between simulation and experiment near the outer borders of zones III and IV. Since the thickness of the applied photoresist amounted to 6.5 μm and no deposition over the resist walls was observed, which would yield to connecting neighboring Cu-lines, the maximum experimental deposit thickness cannot be higher than the resist thickness, This agrees with the actual measured thicknesses; hence thickness values near the edges of zone III and zone IV were overestimated by the simulation.

Experimentally, somewhat higher thickness values were measured for the right side of the wafer (vertically edges of the zones II and IV compared to the vertically edges of the zones I and III) than for the left side, This is related to conditions of air agitation within the electrolyte, which is most effective down in the electrolytic cell resulting in higher Cu-deposit thicknesses on those parts of the wafer which have been placed down there during deposition.

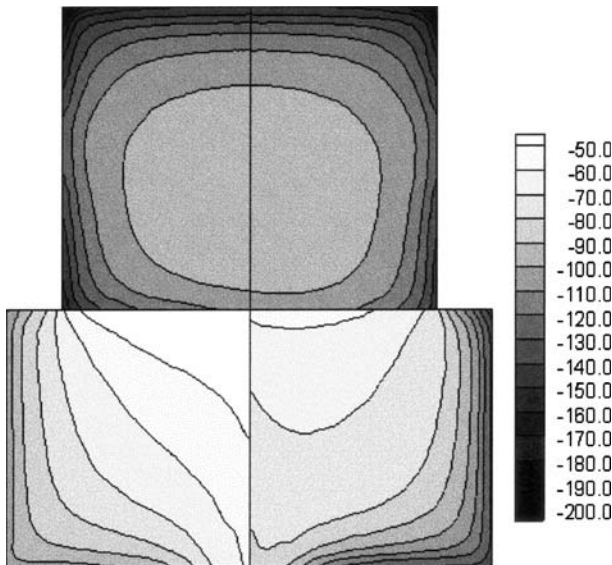

Fig. 7. Macro-scale current density distribution (in A m^{-2}) over zones I, II, III and IV – surface active fractions from Table 1.

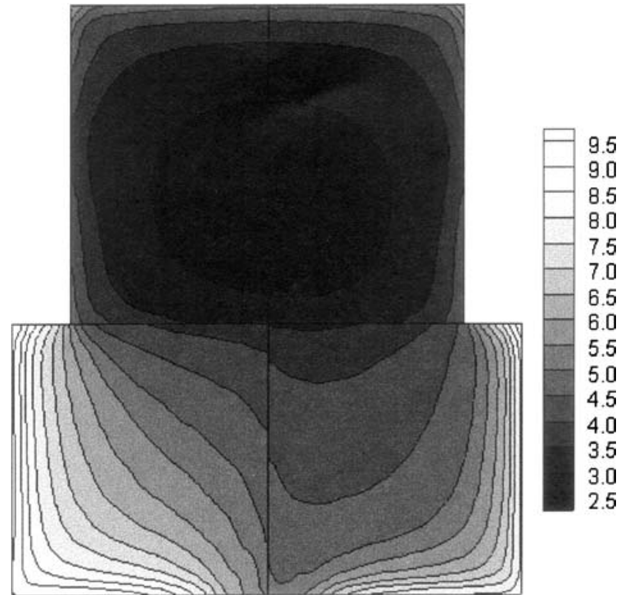

Fig. 8. Simulated layer thickness distribution over the patterned zones I, II, III and IV (in μm) – surface active fractions from Table 1.

5.4. *Comparison with simulation results for a uniform wafer pattern*

Simulated current density and thickness distribution were also performed for a wafer with uniform surface active fraction θ over each zone (Figures 11 and 12). In

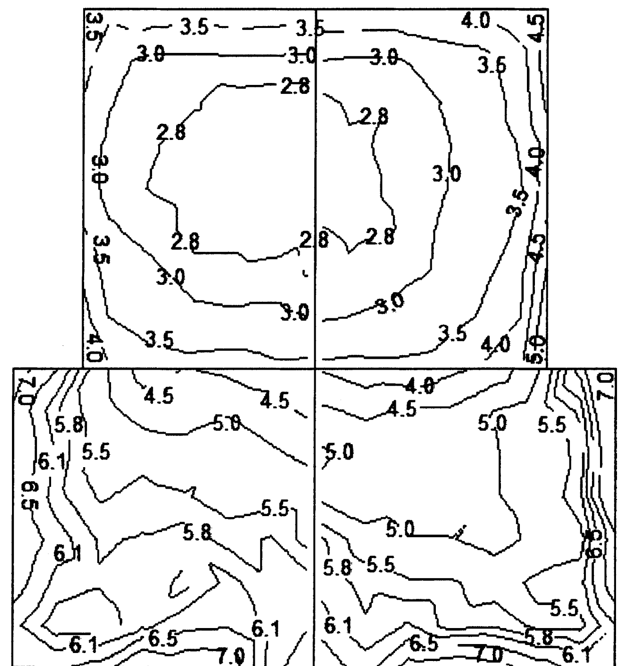

Fig. 9. Experimental layer thickness distribution (XRF-measurements). Values are in μm – surface active fractions from Table 1.

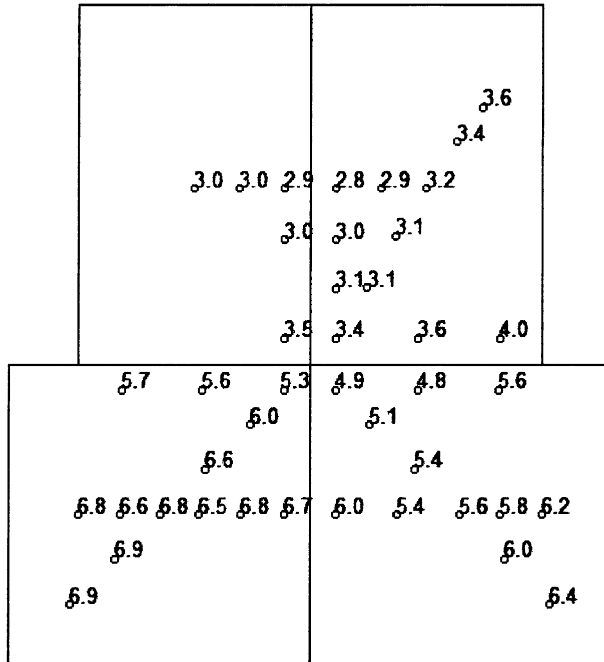

Fig. 10. Local thickness experimentally obtained from AFM studies for selected positions on the patterns. Values are in μm – surface active fractions from Table 1.

order to obtain the same total electro-active surface as for the wafer surface specified in Table 1, the uniform θ value is taken as 0.35. Both the current density and layer thickness distributions tend to be more uniform than for the non-uniform wafer pattern (see Figures 7 and 8). These results clearly illustrate the additional challenge encountered in producing uniform deposit thickness distributions on non-uniform wafer patterns.

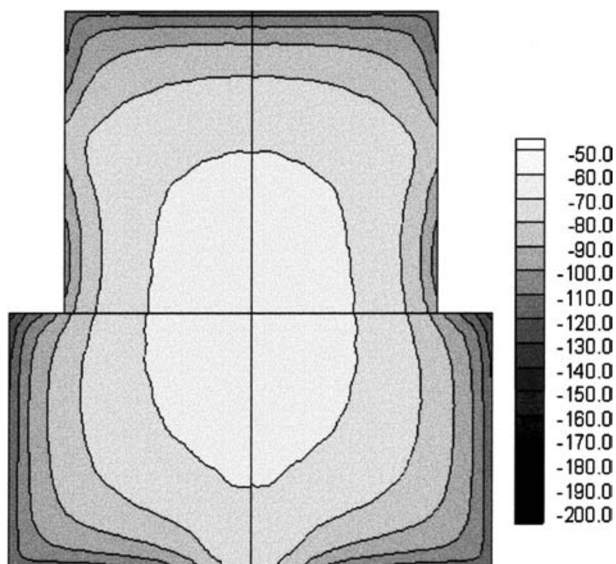

Fig. 11. Macro-scale current density distribution (in A m^{-2}) over zones I, II, III and IV – uniform surface active fraction = 0.35.

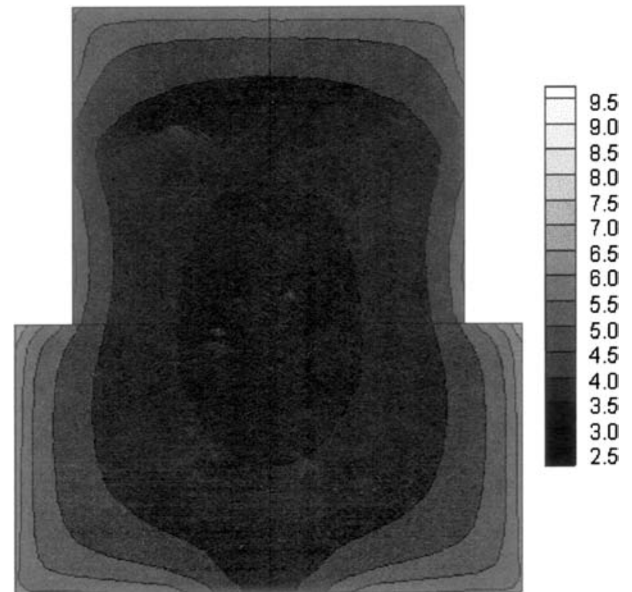

Fig. 12. Simulated layer thickness distribution over the patterned zones I, II, III and IV (in μm) – uniform surface active fraction = 0.35.

5.5. *Discussion of the thickness distribution*

Both the simulated and the experimental results indicate that electrodeposition of the patterned wafer resulted in non-uniform growth rates of the Cu-deposit over the wafer surface. First of all, an edge effect is observed, i.e. the largest deposit thickness occurs close to outer edges and corners. The non-uniformity of the current density and thickness distribution between the various patterns, as simulated and experimentally confirmed, indicates a limited impact of the current thief, although it receives the major part of the current (0.55 A compare to 0.49 A for the wafer, see Table 2). Obviously, the large area of photoresist surrounding the four patterned zones limits the efficiency of the current thief. Since this is well-down for electrodeposition and therefore, in general, outer edges of an electrodeposited sample are considered not to be representative for the remaining sample, the edge-effect will not be discussed further.

Disregarding the edge effect, the thickness appears to be non-uniform within one and the same zone of Cu-line patterns, but even larger thickness differences between the four differently patterned zones were found. The smallest deposit thickness was determined within the patterns of zone I and zone II, where Cu-line widths were equal to interline distances, i.e. conducting and non-conducting areas equal in size alternate with each other. In the case of larger non-conducting areas, either due to increased distances between the lines (zone III) or interruptions in the lengths of lines (zone IV), the Cu-deposit grows thicker. The thickness of Cu-line patterns in zones I and II decreases from all borders of I and II to the middle of the total range of I and II; there the thickness is almost uniform. In zone III, the thickness decreases from the outer edges towards the

center of the wafer; a similar behavior is observed for zone IV. The thickness in both the middle of zone III and the middle of zone IV is almost uniform.

The results suggest that the thickness uniformity is mainly determined by the active area fraction [7, 8, 17] and differences in line width and interline spacing are less important, if the active area fraction remains the same (cf. zones I and II). Comparing Cu-line patterns with the same line dimensions, but different active area fraction (cf. zones II and III), it is observed that sparsely populated patterns, i.e. isolated lines in zone III, grow thicker than Cu-lines which are closer to each other, like in zone II. This is attributed to increased local current densities due to current crowding [17, 18] in isolated lines surrounded by a large nonconducting area (photoresist).

Furthermore, the results indicate that the ratio between active area fractions of neighboring zones is important [23]. Increasing differences between adjacent zones in terms of their active-area-fraction result in increasing thickness variations at the border between the various zones. For example, the border between zone I and II is not obvious from the thickness distribution due to identical active-area-fraction of the two neighboring zones (as mentioned above, differences in the line dimensions, do not seem to affect the thickness). Also, the thickness distribution across the border between zones III and IV is relatively uniform due to small differences in the active-area-fraction there. In contrast, drastic thickness changes are observed where zones with quite different active-area-fractions meet (borders between I and III, and II and IV, respectively).

The non-uniform current distribution over the lithographic patterns on a wafer is expected to be caused not only by the active-area-density effect as mentioned above, but also by pattern driven mass-transport effects [8, 15, 24]. Mass transfer influences on the deposition uniformity depend on the relative sizes of individual features on the substrate (feature-scale effect). Such mass transfer effects in patterned electrodeposition applications are likely to attenuate or reduce the macro-scale non-uniformity [8].

These pattern-driven mass transfer effects are most probably the main reason for the observed differences between the simulated and measured layer thickness distribution, since mass transfer effects were not considered for the simulations. It is not a coincidence that the overprediction of the deposit thickness by the simulations is mainly situated at the outer edge areas of zone III, since the local (crowded) current density on these patterns is the highest of the entire wafer surface (up to 600 A m^{-2}, compared to for example 380 A m^{-2} in zones I and II), hence the most susceptible to mass transfer limitations.

6. Conclusions

The current density distribution over a resist-patterned wafer was simulated for a Cu-electrodeposition process from an industrially relevant electrolyte. The corresponding deposit thickness distribution was calculated from the simulation results and found to be in very good agreement with the experimentally determined thickness distribution over the wafer. The observed non-uniform thickness distribution is related to the geometrical arrangement of the various Cu-patterns on the wafer surface. Parallel Cu-lines, which were arranged with various line dimensions in different zones on the wafer, caused a non-uniform active area density over the wafer surface which yielded pattern dependent growth behavior.

The obtained agreement proves that potential model simulations, which take into account the local surface active fraction in the boundary conditions, yield accurate deposit thickness distribution results, provided that mass transfer limitations remain negligible. Hence this type of 3D simulation software tool can supplement or even substitute experimental studies for optimizing the cell/cathode configuration used for plating non-uniformly patterned wafers.

References

1. S. Mehdizadeh, J. Dukovic, P.C. Andricacos, L.T. Romankiw and H.Y. Cheh, *J. Electrochem. Soc.* **137** (1990) 110.
2. T.P. Moffat, J.E. Bonevich, W.H. Huber, A. Stanishevsky, D.R. Kelly, G.R. Stafford and D. Josell, *J. Electrochem. Soc.* **147** (2000) 4524.
3. T.O. Drews, J.C Ganley and R.C. Alkire, *J. Electrochem. Soc.* **150** (2003) C325.
4. D. Josell, D. Wheeler, W.H. Huber and T.P. Moffat, *Phys. Rev. Lett.* **87** (2001) 016102/1–4.
5. A. Radisik, A.C. West and P.C. Searson, *J. Electrochem. Soc.* **149** (2002) C94.
6. M. Kang, M.E. Gross and A.A. Gewirth, *J. Electrochem. Soc.* **150** (2003) C292.
7. S. Mehdizadeh, J. Dukovic, P.C. Adricacos, L.T. Romankiw and H.Y. Cheh, *J. Electrochem. Soc.* **139** (1992) 78.
8. S. Mehdizadeh, J. Dukovic, P.C. Andricacos P, L.T. Romankiw and H.Y. Cheh, *J. Electrochem. Soc.* **140** (1993) 3497.
9. M. Datta and D. Landolt, *Electrochimica. Acta* **45** (2000) 2535.
10. Y.-J. Tan and K.Y. Lim, *Surface Coatings Technol.* **167** (2003) 255.
11. H. Shih and H.W. Pickering, *J. Electrochem. Soc.* **133** (1986) C325.
12. F. Jagush and R.E. White, *J. Electrochem. Soc.* **137** (1990) 1846.
13. Y.S. Choi and T. Kang, *J. Electrochem. Soc.* **143** (1996) 480.
14. S. Mehdizadeh and J.O. Dukovic, *Transient plating-rate distribution on resistive films with point contact terminals*, Extended Abstracts of the 184th Meeting of the Electrochemical Society, 93–2, IBM J., 1997 Abstract No. 210.
15. G. Ritter, P. McHugh, G. Wilson and T. Ritzdorf, *Solid State Electron.* **44** (2000) 797.
16. M. Purcar, B. Vanden Bossche, L Bortels, J Deconinck and G. Nelissen, *J. Electrochem. Soc.* **151** (2004) D78.
17. G.K.K. Poon and D.J. Williams, *J. Electron. Manufact.* **8** (1998) 15.
18. L.T. Romankiw, *Electrochim. Acta* **42** (1997) 2985.
19. J. Deconinck, *Current Distributions and Electrode Shape Changes in Electrochemical Systems*, Lecture Notes in Engineering Vol. 75, (Springer Verlag, Berlin, 1992), p. 86.
20. C.A. Brebbia and J. Dominguez, *Boundary Elements – An Introductory Course* (Computational Mechanics Publications, McGraw-Hill Book Company, London, 1987), p. 52.
21. J.J. Dongarra and D.W. Walker, *Siam Rev.* **37** (1995) 151.

22. A.N. Athanasiadis and H. Deconinck, *Int. J. Numer. Meth. Eng.* **58** (2003) 301.
23. T. Park, T.E. Tugbawa and D.S. Boning, Proceedings of IEEE 2001, 274.
24. K. Leyendecker, W. Bacher, W. Stark and A. Thommes, *Electrochim. Acta* **39** (1994) 1139.
25. K. Pantleon and M.A.J. Somers, *J. Electron. Mater.* (2004) in press.
26. J.S. Newman, 'Electrochemical Systems', 2nd edn., (Prentice-Hall, Englewood Cliffs, New Jersey, 1991), p. 186.